Metals and Materials International (2018) 24:1422–1431
https://doi.org/10.1007/s12540-018-0147-y

Influence of Cooling Condition of Casted Strips on Magnetic Properties of Nd–Fe–B Sintered Magnets

Hwaebong Jung[1] · Sumin Kim[1] · Hongjae Moon[1] · Yoon S. Oh[2] · Young-Joo Lee[2] · Hyun-Sook Lee[1] · Wooyoung Lee[1]

Received: 22 February 2018 / Accepted: 13 May 2018 / Published online: 8 June 2018
© The Korean Institute of Metals and Materials 2018

Abstract
We investigated the additional (secondary) cooling effect of casted strips on the magnetic properties of Nd–Fe–B sintered magnets. The Nd–Fe–B sintered magnets were fabricated with the casted strips prepared without and with additional cooling. Additional cooling was achieved by blowing Ar gas at various pressures (0.1, 0.3, and 0.6 MPa) on the free-side surface of the strips during the strip-casting process. The higher magnetic properties of H_c, B_r, and $(BH)_{max}$ of the final Nd–Fe–B sintered magnets were obtained for 0.1 MPa rather than for 0.0 MPa. The best microstructure of the columnar grains in the casted strips was produced with the aid of a lower pressure of gas on the free-side surface. It was found that the microstructure of the strips affects the distribution of grains grown in the sintered magnets. This report demonstrates that the improved magnetic performance of Nd–Fe–B sintered magnets was achieved via additional gas cooling.

Keywords Nd–Fe–B sintered magnet · Strip casting · Additional cooling · Magnetic properties

1 Introduction

Nd–Fe–B sintered magnets, developed by Sagawa et al. [1], are widely used because of their outstanding magnetic performance. A theoretical maximum energy product $(BH)_{max}$ of 64 MGOe can be achieved when the magnet is composed of the single crystalline $Nd_2Fe_{14}B$ phase and all grains are perfectly oriented along their easy magnetization direction [2, 3]. However, the highest experimental value of $(BH)_{max}$ reported for Nd–Fe–B sintered magnets so far is 56.7 MGOe [4], which is lower in value than the theoretical limit. To improve the magnetic properties, several methods have been applied, such as the addition of other elements (Dy, Pr, Nb, etc.) [5–10], development of new techniques (strip casting, hydrogen decrepitation, jet-mill, magnetic pressing, etc.) [11–19], and control of the heat treatment condition (sintering temperature [20], high-magnetic-field annealing [21], spark plasma sintering [22], etc.).

Among these methods, the strip casting (SC) technique offers many advantages such as sparing rare-earth resources, homogenizing the lamellar structures, and suppressing the formation of α-Fe dendrites [4, 18, 19]. It has been found that the microstructure of the Nd–Fe–B starting alloy plays an important role in determining the magnetic properties of the sintered Nd–Fe–B magnets [18, 19, 24, 25]. Homogenous and fine lamellar structures with a spacing of ~ 3 μm and an average width of ~ 150 nm and without significant precipitation of α-Fe are required [19]. This is because the microstructure and phase structure of the starting alloys are advantageous for the milling of the alloy after hydrogen decrepitation and improving the sinterability of the magnets [19]. The formation of α-Fe, fine columnar crystals, and the Nd-rich phase of a thin layer depends on the solidification rate during casting [18]. Thus, significant effort has been dedicated to control the solidification rate in order to obtain optimized microstructures for the casted strips by adjusting the wheel speeds [15, 18, 25], strip thicknesses [24, 26], and melting temperatures [23] during the strip-casting procedure.

Despite such efforts, it is inevitable that the lamellar spacing becomes larger at the free side of the strips compared to that at the wheel side. This is caused by the fact that the

✉ Hyun-Sook Lee
h-slee@yonsei.ac.kr

✉ Wooyoung Lee
wooyoung@yonsei.ac.kr

[1] Department of Materials Science and Engineering, Yonsei University, Seoul 03722, Republic of Korea

[2] Metallic Materials Research Group, Research Institute of Industrial Science and Technology, Pohang 37673, Republic of Korea

columnar structures, beginning at the nucleation site at the wheel side of the strips, usually grow within a cone with an open angle of 60°–80° towards the free side [19]. Therefore, a high density of fine lamellar structures is distributed near the wheel side. In this work, we attempted to control the formation of homogenous and fine lamellar structures by adding secondary cooling for the first time. The additional cooling was achieved by blowing Ar gas on the free side of the strips during casting. By applying gas cooling process at the free side, we intended to prevent the enlargement of lamellae to the free side by generating the nucleation sites, and to produce much oftowards the free side fine lamellar structures near the wheel and the free sides. The influence of additional cooling on the microstructure of the casted strips and on the magnetic properties of Nd–Fe–B sintered magnets was investigated.

2 Experimental Procedures

The nominal composition of starting alloy was $Nd_{13.9}Fe_{80.8}Co_{1.1}Cu_{0.2}Al_{0.5}Nb_{0.2}B_{3.4}$ (at%). According to previous reports [27, 28], the fraction of Nd-rich phase could be increased by lowering B content in Nd–Fe–B magnets and their magnetic properties were significantly degraded at the B content below 3–4 at%. In order to provide sufficient amount of Nd-rich GB phases in the starting alloy, we intentionally designed it to have low B content of ~ 3.4 at%, which is out of optimal boron stoichiometry of ~ 6 at% in $Nd_2Fe_{14}B$. The purpose is to efficiently observe the microstructural change (nucleation site, growth direction, lamellar spacing etc.) of the lamellar structure affected by the additional cooling in the casted strips, even though the low B content results in the deterioration of the magnet performance. The Cu and Al elements were used to enhance a wetting behavior of liquid Nd-rich phase during sintering and thus to produce smooth the grain boundaries [29]. The Nb element was used as a grain refiner or grain inhibitor [29].

The starting alloys were prepared by a strip-casting technique. The raw materials were melted by induction heating up to 1550 °C and the molten alloys were poured onto the tundish. The casted strips were produced on a rotating copper roller. A Cu roller with a diameter of 30 cm was cooled by water flow. The optimal wheel speed was determined by varying between speeds of 1.5, 2.0, 2.5, and 3.0 m/s. To investigate the additional cooling effect, high-purity Ar gas (99.99%) was blown on the free side of the strip during the strip-casting process at various pressures: 0.1, 0.3, and 0.6 MPa. The Ar gas pressures were adjusted via the regulator of the gas tank and the flow rates were not controlled during the blow of gas. A schematic featuring the strip-casting process including the additional cooling by blowing Ar gas through the gas nozzle is presented in Fig. 1. The casted thin Nd–Fe–B flakes were crushed into coarse powders by the hydrogen decrepitated (HD) technique. The HD powders were pulverized into finer powders with an average particle size of 3.2 μm through jet-milling in a nitrogen atmosphere.

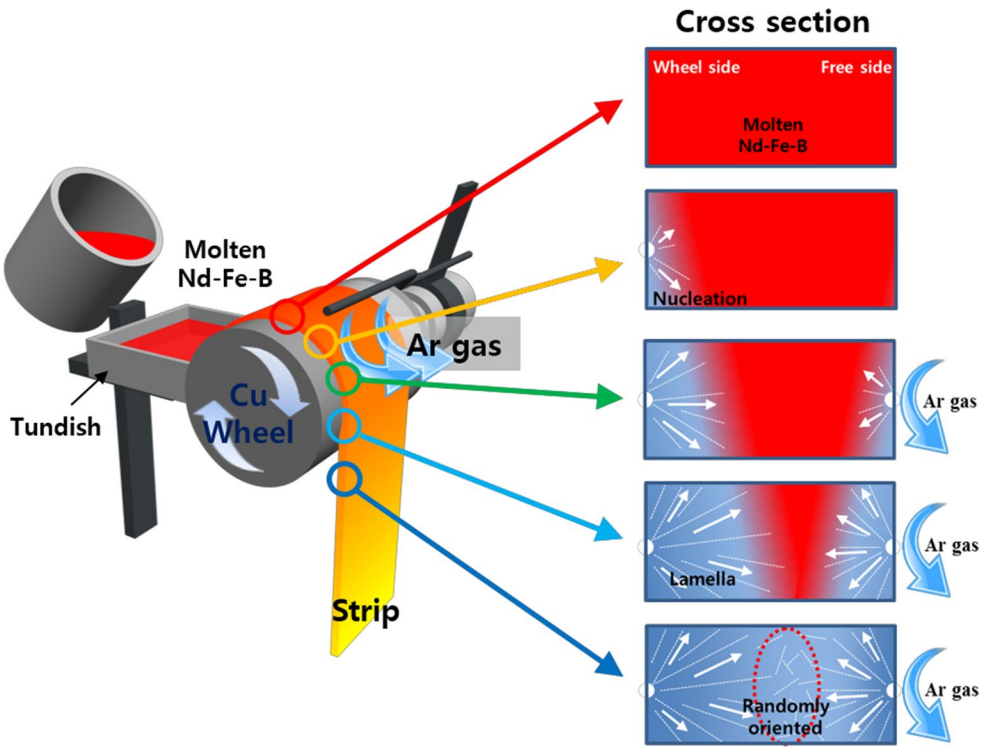

Fig. 1 A schematic of the modified strip-casting apparatus including Ar gas cooling system and the microstructural change of the casted strip during the solidification process at both sides of the strips: wheel side and free side

The fine powders were compacted to the dimensions of 20.4 mm × 15.6 mm × 17.4 mm under an applied pressure of 62 MPa in the presence of a 2 T magnetic field in an argon atmosphere at room temperature. The compaction density was about 2.8 g/cm^3. The green compacts were sintered at various temperatures of 1080, 1100, and 1120 °C for 30 min in vacuum, followed by furnace cooling to 25 °C under a flow of Ar gas. Finally, the sintered magnets were annealed in two steps: at 850 °C for 1 h and at 550 °C for 2 h. The sintered density of the final bulk magnets was determined by the Archimedes method.

The phases and crystalline orientation of the Nd–Fe–B strips were characterized using X-ray diffraction (XRD, D/Max-2500 VL-PC, Rigaku) with Cu Kα radiation. The microstructural characterization of the strips and sintered magnets were investigated by scanning electron microscopy (SEM, JSM 7600F, JEOL). The chemical analyses were performed with an energy-dispersive X-ray spectroscope (EDX). For the microscopic analysis of the sintered magnets, they were demagnetized at 300 °C for 3 h under vacuum. To determine their magnetic properties, they were magnetized using a magnetizer. Magnetic properties of the Nd–Fe–B sintered magnets were assessed using a *B–H* loop tracer (Robograph HC and Robograph RE, ECKEL) at room temperature.

3 Results and Discussion

Figure 1 presents a schematic illustration of the modified strip-casting apparatus including the Ar gas cooling system and the solidification process of the Nd–Fe–B strips. The molten alloys are contacted with the rotating Cu wheel and passed through the Ar gas nozzle. The nucleation sites for solidification are formed at the wheel side of the strips. Starting from the nucleation sites, the lamellar structures grow following the heat flow direction as illustrated in Fig. 1. The lamellar structure is composed of columnar grains of the hard magnetic $Nd_2Fe_{14}B$ phase. The Nd-rich phase is distributed along the boundaries of the columnar grains. During Ar gas flow, nucleation sites were also formed at the free side of the strips due to the cooling effect and lamellar structures grew, as described in the schematic illustration in Fig. 1. Consequently, randomly oriented lamellar structures appeared on the inner side of the strips since the heat flow directions at the wheel and free side were opposite.

In order to investigate the effect of additional gas cooling on the microstructures of the casted strips, we first optimized the wheel speed before applying Ar gas cooling. Figure 2 shows the cross-sectional SEM images of the casted strips produced at the various wheel speeds of 1.5, 2.0, 2.5, and 3.0 m/s without Ar gas cooling. Nucleation sites were detected at the wheel side of the strips. As Fig. 2 shows, different distributions of nucleation sites and lamellar structures were observed for different speeds. The

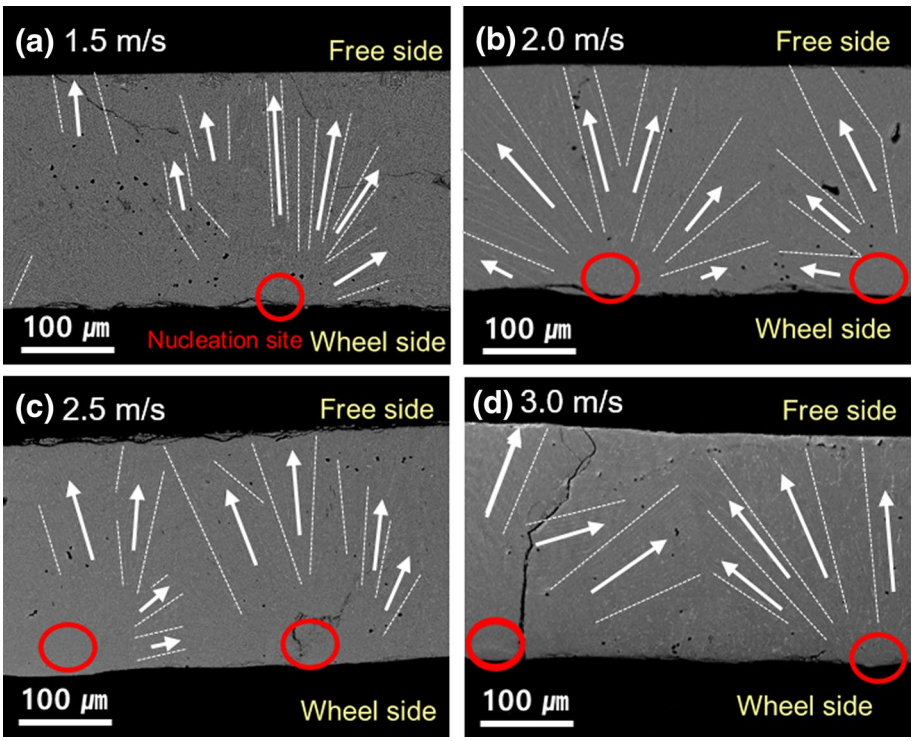

Fig. 2 Cross-sectional SEM images of the casted strips prepared at the wheel speeds **a** 1.5, **b** 2.0, **c** 2.5, and **d** 3.0 m/s without Ar gas cooling

average intervals of lamellar structures were estimated to be ~ 3.3 μm for 1.5 m/s, ~ 3.0 μm for 2.0 m/s, ~ 4.6 μm for 2.5 m/s, and ~ 5.0 μm for 3.0 m/s. Comparison of Fig. 2a–d shows that relatively good microstructure, which has smaller lamellar spacing and homogenous distribution of the lamellar structure, is obtained at 2.0 m/s (Fig. 2b).

The phases and crystalline orientation of the strips prepared at different wheel speeds without Ar gas cooling were characterized using XRD analysis. The XRD patterns, obtained from the wheel-side surface of the strips, are shown in Fig. 3a. The diffraction peaks were indexed to the crystal structures of $Nd_2Fe_{14}B$ and α-Fe phases. The reflection peak of (110) for the α-Fe phase was indexed at the same 2θ as that of (006) for the $Nd_2Fe_{14}B$ phase, as shown in Fig. 3a. However, other notable peaks for α-Fe phase were not observed. The strong intensity of the XRD peaks from the (00l) ($l=2n$) planes of $Nd_2Fe_{14}B$ phase indicates that the c-axis of $Nd_2Fe_{14}B$ phase prefers to align along the direction perpendicular to the wheel-side surface of the casted strips. This is consistent with the results reported by Hattori et al. [30]. As the wheel speeds varied, the degree of random orientation of $Nd_2Fe_{14}B$ phase near the wheel-side surface was investigated by comparison of the intensity ratio (I(105)/I(004)) of the XRD peaks of (105) and (004) instead of I(105)/I(006). This is because the intensity at $2\theta=$ ~ 44.6° includes the two phases of $Nd_2Fe_{14}B$ (006) and α-Fe (110). The intensity ratios of I(105)/I(004) as a function of the wheel speed are presented in Fig. 3b, which shows the lowest value at 2.0 m/s. This indicates that the smaller random orientation of the magnetic phase is observed at 2.0 m/s. According to the results of SEM (Fig. 2) and XRD (Fig. 3) analyses, we choose 2.0 m/s as the optimal wheel speed.

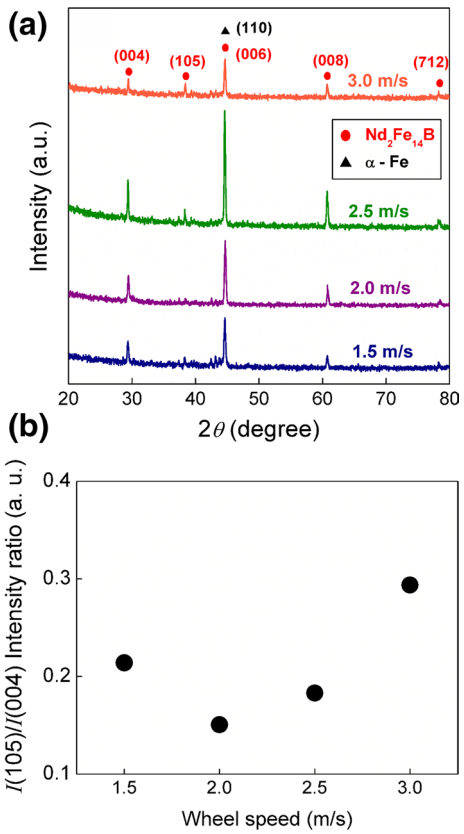

Fig. 3 **a** XRD patterns of the casted strips prepared at the wheel speeds of 1.5, 2.0, 2.5, and 3.0 m/s without Ar gas cooling. **b** Intensity ratio between the XRD peaks of I(105) and I(004) as a function of the wheel speed

The casted Nd–Fe–B thin flakes prepared at the wheel speed of 2.0 m/s were pulverized into finer powders using HD and jet-milling processes. The average particle size of the fine powders was about 3.2 μm. In order to find the optimum sintering temperature, the green compacts of the fine powders were sintered at various temperatures of 1080, 1100, and 1120 °C for 30 min. The final bulk magnets were prepared by a two-step annealing procedure after sintering. The sintered density and the magnetic properties of the final Nd–Fe–B magnets are displayed in Fig. 4a–c, respectively. As Fig. 4 shows, the highest values for the density and magnetic properties were obtained at the sintering temperature of 1120 °C.

Figure 5 shows the effect of wheel speeds of the casted strips on the magnetic properties of the final magnets sintered at the optimal temperature of 1120 °C. The magnetic properties H_c, B_r, and $(BH)_{max}$ for the Nd–Fe–B sintered magnets were obtained from the demagnetization curves in Fig. 5a and are displayed in Fig. 5b–d. As the wheel speed increases to 2.5 and 3.0 m/s, the magnetic performances were degraded. This was due to the appearance of a larger amount of the α-Fe phase at the wheel speeds of 2.5 and 3.0 m/s, which was observed using XRD measurements (data not shown here). The large amount of decrease in B_r could be related to the increase of α-Fe phases that deteriorates the magnetic alignment [16]. Higher magnetic properties were observed at the wheel speed of 2.0 m/s. Thus, we chose the optimal wheel speed of 2.0 m/s.

Figure 6b–d show the cross-sectional SEM image of the casted strips prepared with additional cooling at the free side of the strips during the strip casting process as shown in Fig. 1. Here, the wheel speed was 2.0 m/s and various Ar gas pressures of 0.1, 0.3, and 0.6 MPa were applied. In order to assess the additional cooling effect on the microstructure of the casted strips, the cross-sectional SEM image of the casted strips prepared without Ar gas cooling (0.0 MPa) is presented again in Fig. 6a, which is the same image as Fig. 2b. In the absence of Ar gas pressure (0.0 MPa), the nucleation sites were produced only at the Cu wheel side (Fig. 6a). However, in the presence of Ar gas pressure of 0.1–0.6 MPa, they appeared both at the wheel and at the free sides of the strips (Fig. 6b–d). In particular, at 0.1 MPa (Fig. 6b), the lamellar structures grew

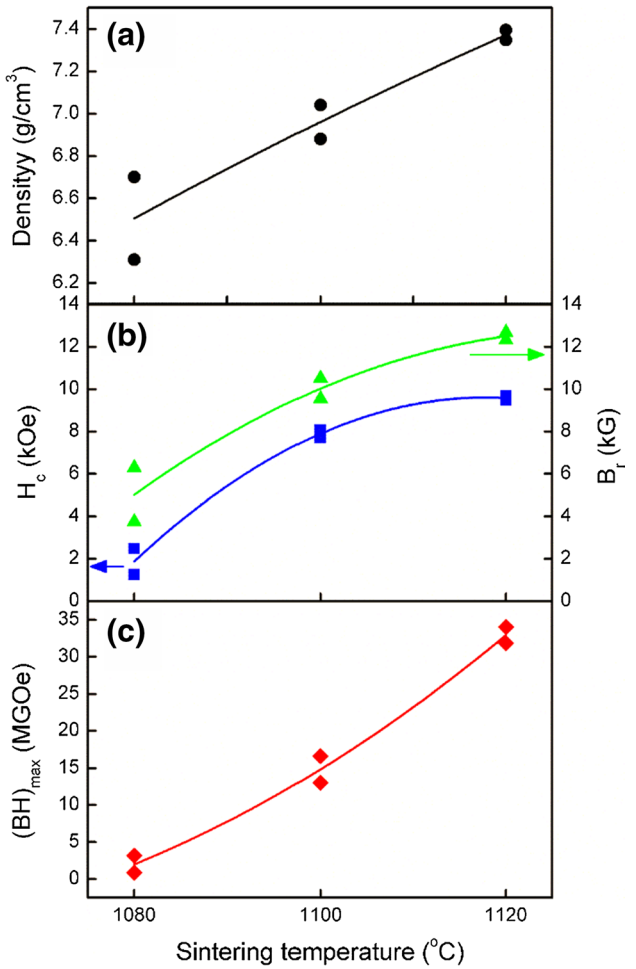

Fig. 4 **a** Density and **b**, **c** magnetic properties H_c, B_r, and $(BH)_{max}$ of the Nd–Fe–B sintered magnets as a function of the sintering temperature. The casted strips were fabricated at the wheel speed of 2.0 m/s without Ar gas cooling. Solid lines drawn in (**a**–**c**) are guide to the eyes

along both directions from the nucleation sites generated at the wheel and free sides and randomly oriented lamellar structures existed in the inner side. This is consistent with the prediction described in the schematic illustration in Fig. 1. As the Ar gas pressure increased to 0.3 and 0.6 MPa, the lamellar structures were not well distinguished, the amount of lamellae was significantly reduced, and randomly oriented lamellar structures were distributed along the wide part of the strips (Fig. 6c, d). The average intervals of the lamellar structures of the strips prepared without gas cooling (0.0 MPa) was about ~ 3.0 μm. When additional gas cooling was applied, the average intervals increased: ~ 3.5 μm at 0.1 MPa. However, a noteworthy feature is that the distance between columns, which begin at the nucleation site and are composed of lamellae, decreases at 0.1 MPa compared to that at 0.0 MPa.

According to the SEM results in Fig. 6, the number and interval of nucleation sites at the wheel side are changed because of generation of nucleation sites at the free side. This means that the crystalline orientation of $Nd_2Fe_{14}B$ phase is affected by the additional gas cooling. Thus, we investigated the variation of crystalline orientation of $Nd_2Fe_{14}B$ phase depending on the gas pressures. Figure 7a shows the XRD patterns obtained from the wheel-side surface of the strips prepared without and with Ar gas cooling at the wheel speed of 2.0 m/s. The XRD patterns show that the (00*l*) peaks were still strong, indicating that the *c*-axis-oriented $Nd_2Fe_{14}B$ phases grew along the cross-sectional direction of the strip. This is consistent with the previous report [29] that the $Nd_2Fe_{14}B$ phase of the strip has a tendency to align along the c-axis at the wheel surface. However, as the zoomed XRD patterns in the 2θ range of 35°–44° show in Fig. 7b, other crystalline growth directions (*hkl*) of the $Nd_2Fe_{14}B$ main phase besides (00*l*) were observed. These peak intensities increased with increasing gas pressure. The intensity ratio of I(105)/I(004), implying the degree of random orientation (or deviation of the preferred c-axis orientation) of the $Nd_2Fe_{14}B$ phase at the wheel side, was examined, as shown in Fig. 7c. The deviation of c-axis alignment near the wheel side increased at higher gas pressures of 0.3 and 0.6 MPa. Especially, the lowest deviation was observed at 0.1 MPa rather than at 0.0 MPa. This is significant, since the best microstructure in the casted strips can be produced with additional cooling with a lower value of Ar gas pressure.

The final Nd–Fe–B sintered magnets were fabricated using the fine powders produced from the casted Nd–Fe–B thin flakes prepared at different Ar gas pressures. Figure 8 shows the effect of Ar gas pressures on the casted strips on the magnetic properties of the final magnets sintered at 1120 °C. The magnetic properties H_c, B_r, and $(BH)_{max}$ of the Nd–Fe–B sintered magnets were obtained from the demagnetization curves in Fig. 8a and are shown in Fig. 8b–d. According to the results, the highest magnetic properties were obtained for the sintered magnets produced with the casted strips using Ar gas pressure of 0.1 MPa, which showed the best microstructure.

Figure 9 shows the XRD patterns of the final sintered magnets fabricated using the casted strips prepared with various gas pressures of 0.0, 0.1, and 0.6 MPa. The diffraction peaks of the sintered magnets were indexed to the crystal structures of $Nd_2Fe_{14}B$ (ICDD: #01-070-1385), Nd_2Fe_{17} (ICDD: #01-071-8316), α-Fe (ICDD: #01-076-658), and Nd-rich [31] phases. The XRD results indicate that the sintered magnet prepared at 0.1 MPa mainly consists of $Nd_2Fe_{14}B$ phase. However, other phases such as Nd_2Fe_{17}, α-Fe, and Nd-rich phases were found for pressures of 0 and 0.6 MPa. The amount of those phases increases at higher gas pressure of 0.6 MPa. According

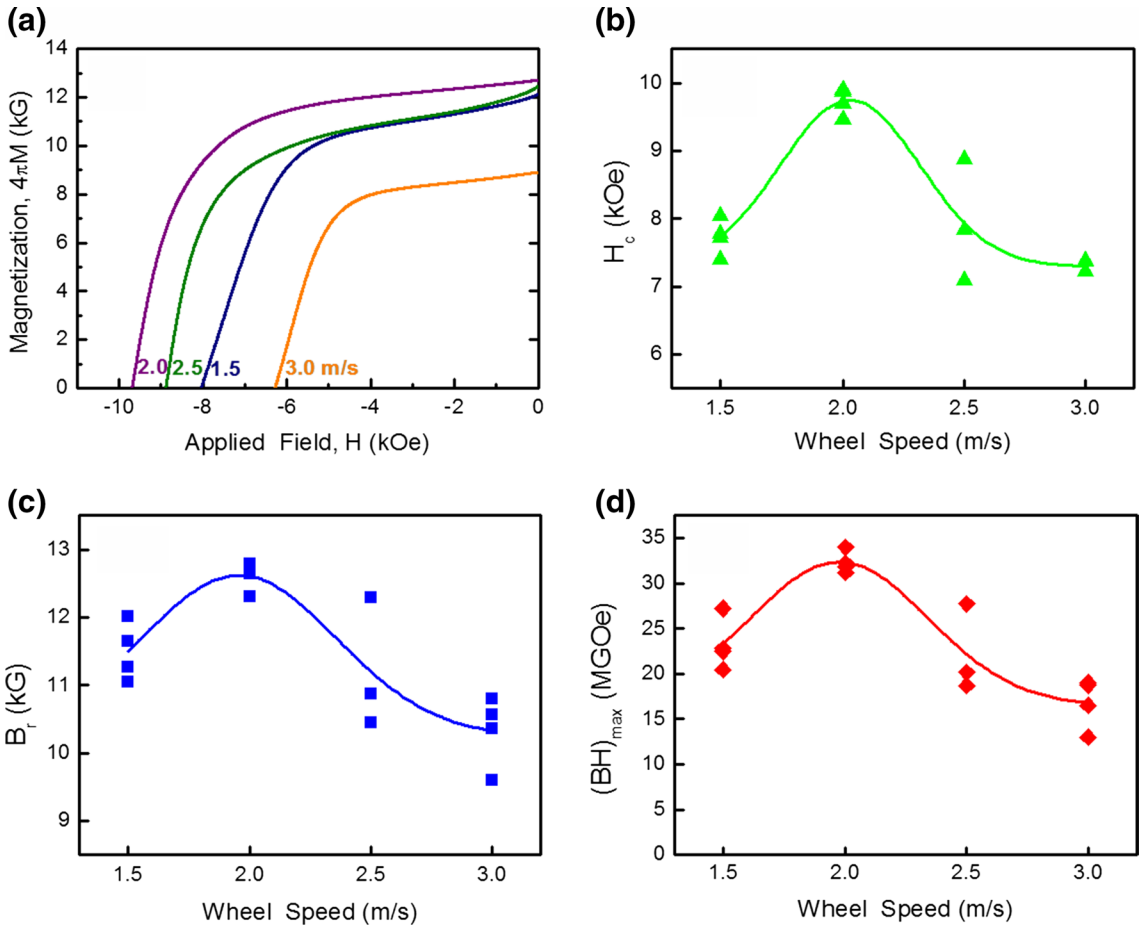

Fig. 5 Effect of the wheel speeds of strips on magnetic properties of the sintered magnets at 1120 °C. **a** Demagnetization curves, **b** coercivity H_c, **c** remanence B_r, and **d** maximum energy product $(BH)_{max}$. Solid lines drawn in (**b**–**d**) are guide to the eyes

to previous works [27, 32], Nd_2Fe_{17} phase can be formed in Nd–Fe–B magnet due to some reasons. First, it is a case that boron content of a starting alloy is lower than the standard stoichiometric atomic fraction of boron (5.88 at%) in $Nd_2Fe_{14}B$ [27]. Second, Nd_2Fe_{17}, α-Fe, and Nd-rich phases can be formed in a melt-spun ribbon during melt spinning or in a casted strip during strip casting [32]. The amount of Nd_2Fe_{17}, α-Fe, and Nd-rich phases increases with increasing cooling speed [32]. Third, an amorphous phase existing in strips or ribbons can be transformed to the Nd_2Fe_{17}, α-Fe, and Nd-rich phases during annealing [32].

The existence of Nd_2Fe_{17} phase in the Nd–Fe–B sintered magnets as seen in Fig. 9 can be attributed to the low boron content (3.4 at%) in the starting alloy regardless of gas pressure for additional cooling. It should be noted that Nd_2Fe_{17} phase was not found in the casted strip (see Fig. 7). We infer that grain growth (phase transformation) of Nd_2Fe_{17} phase from nanocrystalline (or amorphous phase) occurs during sintering. The lowest amount of Nd_2Fe_{17}, α-Fe, and Nd-rich phases was observed in 0.1 MPa. This indicates that the gas pressure of 0.1 MPa can be considered as a moderate cooling.

In particular, the magneto anisotropy of the Nd_2Fe_{17} phase is planar and much smaller than that of $Nd_2Fe_{14}B$ [33]. The Nd_2Fe_{17} phase grains usually act as a nucleation sites of reversal magnetization. Therefore, the presence of Nd_2Fe_{17} phase results in the significantly reduced coercivity as well as the reduced magnetization. From the analysis of XRD results, it is understandable that the highest magnetic performance and remarkably degraded magnetic performance were shown in the cases of 0.1 and 0.6 MPa, respectively, as shown in Fig. 8.

Figure 10a–c show the SEM images of the final sintered magnets fabricated using the casted strips prepared with various gas pressures of 0.0, 0.1, and 0.6 MPa, respectively. Figure 10d shows a magnified view of the SEM image for the 0.1 MPa case, which is circled in Fig. 10b. The precipitations at the pressure of 0.0 and 0.6 MPa could be observed in the SEM images. In order to identify the precipitations in the images, an elemental analysis was performed using an energy-dispersive X-ray spectroscope (data not shown

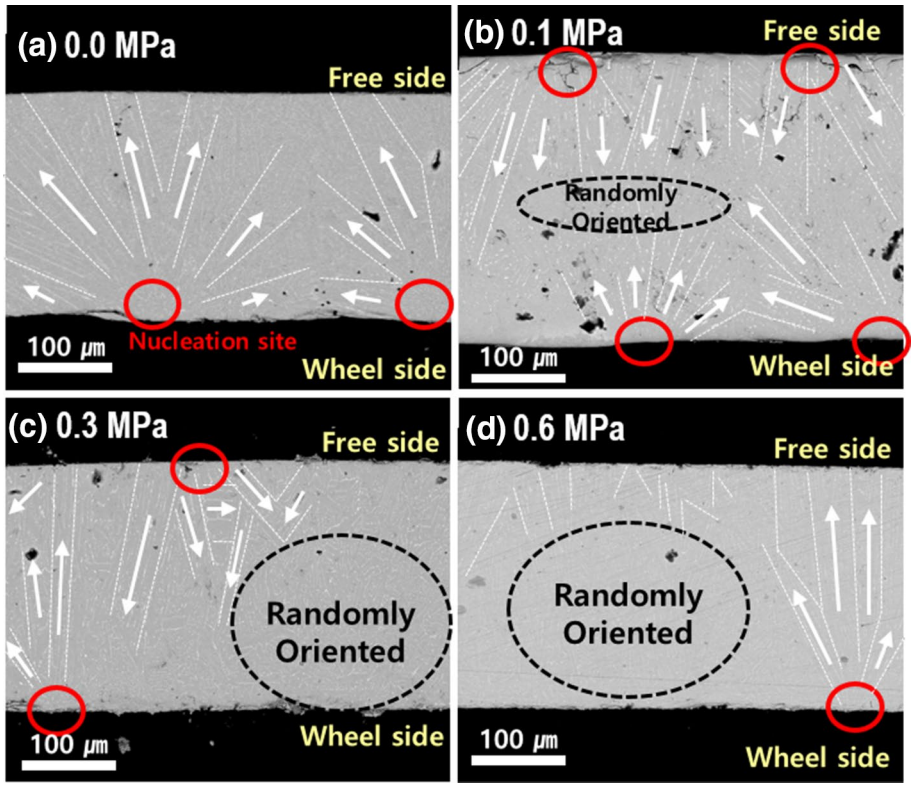

Fig. 6 Cross-sectional SEM images of the casted strips prepared by Ar gas cooling with the pressures **a** 0.0, **b** 0.1, **c** 0.3, and **d** 0.6 MPa at the wheel speed of 2.0 m/s

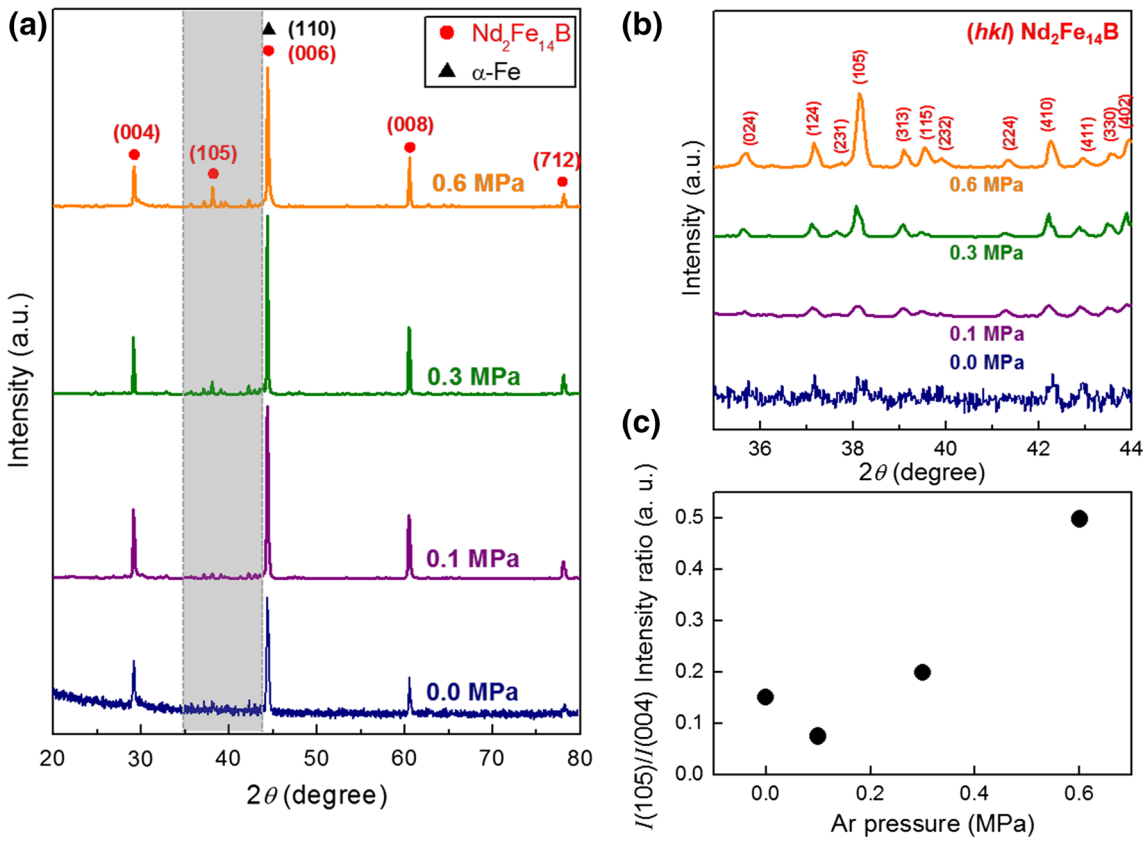

Fig. 7 **a** XRD patterns of the casted strips prepared with Ar gas cooling at various gas pressures of 0.0, 0.1, 0.3, and 0.6 MPa and a wheel speed of 2.0 m/s. **b** Zoomed XRD patterns in the 2θ range of 35°–44° designated with gray in (**a**). **c** Intensity ratio between the XRD peaks of $I(105)$ and $I(004)$

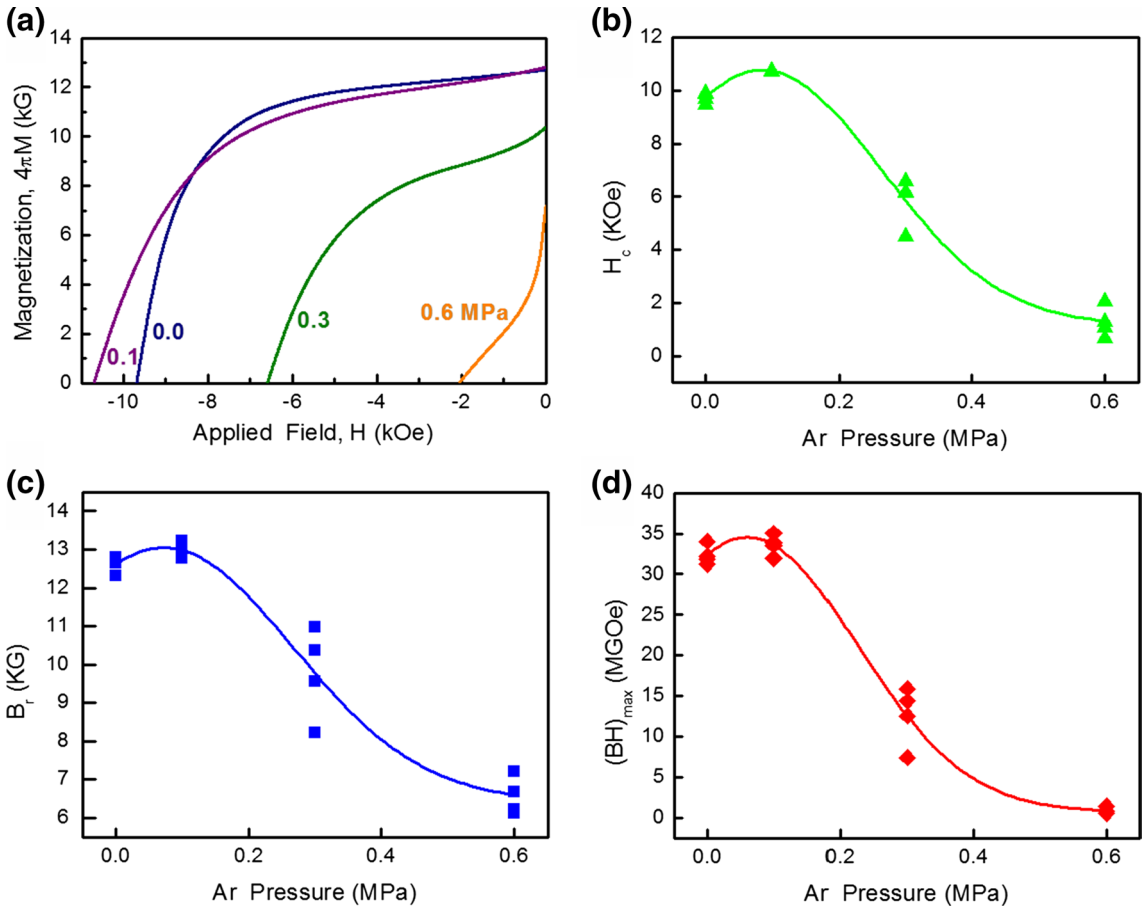

Fig. 8 Effect of the Ar gas pressures on the magnetic properties of the final sintered magnets. **a** Demagnetization curves, **b** coercivity H_c, **c** remanence B_r, and **d** maximum energy product $(BH)_{max}$. Solid lines drawn in (**b**–**d**) are guide to the eyes

here). The EDX analysis implies a Fe-rich phase for dark gray region, a Nd–Fe–B phase for gray region, and a Nd-rich phase for light gray in the SEM images in Fig. 10. Therefore, the chemical analysis showed that the sintered magnet, prepared at a high gas pressure of 0.6 MPa, has large amount of Fe-rich and a-Fe phases, and more precipitates were formed in the sintered magnet prepared at 0.0 MPa compared to 0.1 MPa. The results were consistent with the XRD results as shown in Fig. 9.

According the SEM images in Fig. 10, a continuous thin layer of the intergranular Nd-rich phase surrounding the $Nd_2Fe_{14}B$ grains, which is a key microstructural feature of high coercivity Nd–Fe–B magnets [34], was relatively well defined in the sintered magnets produced with casted strips prepared under gas pressures of 0.0 and 0.1 MPa compared to those prepared under 0.6 MPa. However, most of the grain boundaries in the case of 0.6 MPa were composed of the α-Fe phase, which is a soft magnetic phase that acts as a reverse-domain nucleation site [35]. This resulted in a very low value of H_c, as shown in Fig. 8b. In particular, smaller grains (Fig. 10b) and smoother grain boundaries (Fig. 10d) were observed at 0.1 MPa compared to those at 0.0 MPa (Fig. 10a). These features gave rise to an improved H_c at 0.1 MPa compared to at 0.0 MPa, as shown in Fig. 8b. In addition, a lower fraction of the Fe-rich and α-Fe phases was also observed for 0.1 MPa. The sintered density was estimated at a higher value of 7.6 g/cm^3 at 0.1 MPa than at 0.0 MPa (7.4 g/cm^3), as shown in Fig. 4a. The higher B_r at 0.1 MPa was attributed to the lower fraction of Fe-rich and α-Fe phases and higher sintered density at 0.1 MPa, as shown in Fig. 8c. The $(BH)_{max}$ was also higher at 0.1 MPa due to the higher values of H_c and B_r.

Based on the results of SEM (Fig. 6) and XRD (Fig. 7) of the casted strips, the best microstructures in the casted strip were found to strongly affect the higher magnetic properties in the sintered magnets. The best microstructure of the casted strips could be obtained from an optimal thermal gradient (moderate cooling rate) through the strip, which was produced by additional cooling with a lower gas pressure. Then, the best microstructure of the casted strips stimulated the formation of small grains, a smooth grain boundary, a lower fraction of the Nd_2Fe_{17} and α-Fe phases, and higher

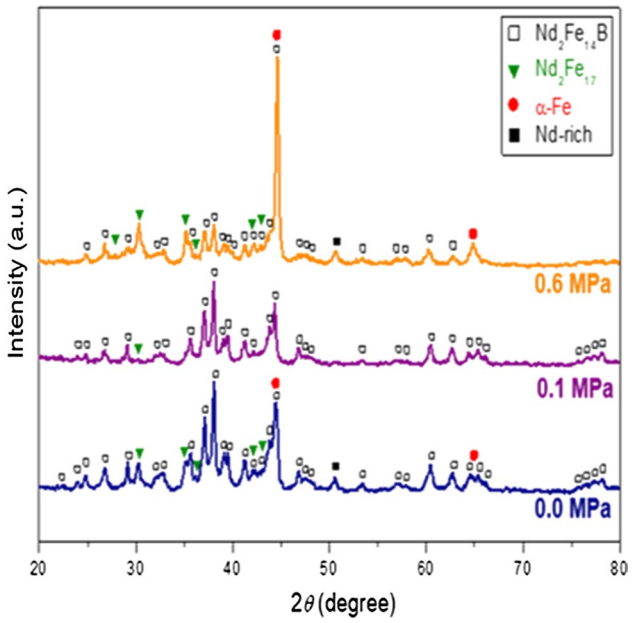

Fig. 9 XRD patterns of the final sintered magnets fabricated using the casted strips prepared with various gas pressures of 0.0, 0.1, and 0.6 MPa

sintered density in the sintered magnets (Fig. 9 and Fig. 10). We found that additional gas cooling at the free side plays an important role in producing good quality of lamellar structures in the casted strips. The lower gas pressure prevents lamellar structure spreading from wheel side to free side with larger lamellar spacing. It was noted that additional gas cooling at the free-side surface of the strips has a positive effect on the hard magnetic properties of the sintered magnets.

4 Conclusions

We investigated the additional cooling effect of casted strips on the magnetic properties of the final sintered Nd–Fe–B magnets. Nd–Fe–B sintered magnets with nominal composition of $Nd_{13.9}Fe_{80.8}Co_{1.1}Cu_{0.2}Al_{0.5}Nb_{0.2}B_{3.4}$ were fabricated by using casted strips prepared without (0.0 MPa) and with Ar gas cooling (0.1, 0.3, and 0.6 MPa). For additional cooling, Ar gas was blown on the free-side surface of the casted strips during the strip-casting procedure and at various gas pressures. The best microstructures of the casted strips with properties such as well-oriented lamellar structures and average lamellar spacing were obtained when 0.1 MPa of Ar gas pressure was applied. It affected the good quality of the microstructure of grains in the sintered magnets. Consequently, the higher magnetic properties H_c, B_r, and $(BH)_{max}$ of the final Nd–Fe–B sintered magnets were produced at 0.1 MPa rather than at 0.0 MPa. This is noteworthy because this is the report on the observation that additional gas cooling on the strip surface is beneficial for improving the magnetic properties of Nd–Fe–B sintered magnets.

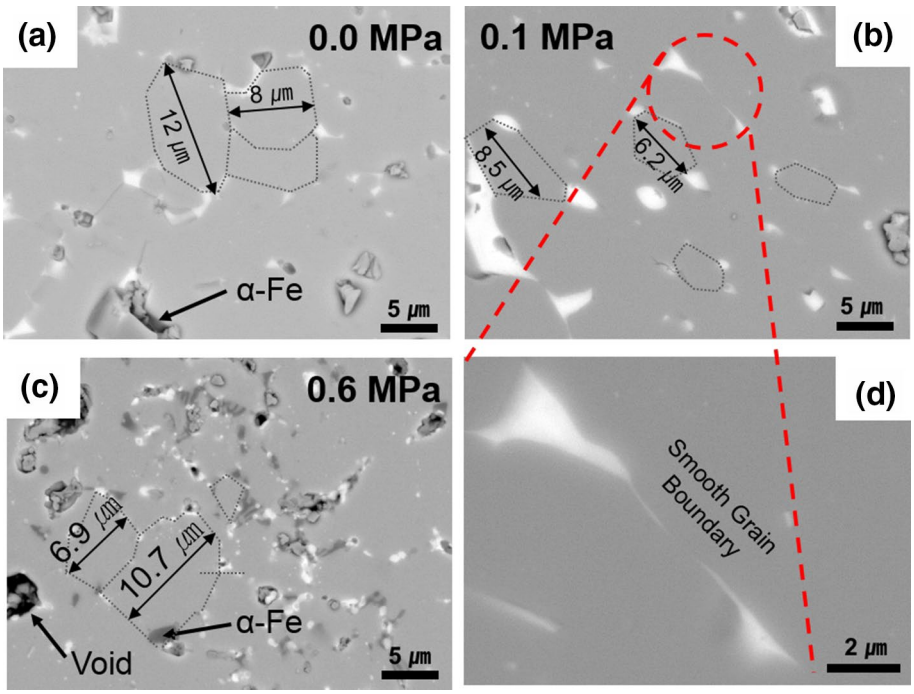

Fig. 10 SEM images of the final sintered magnets fabricated using the casted strips prepared with various gas pressures of **a** 0.0, **b** 0.1, and **c** 0.6 MPa. A magnified view of the circles area in (**b**) is shown in (**d**)

Acknowledgements This work was supported by the Priority Research Centers Program (2009-0093823) through the National Research Foundation of Korea (NRF). H-S Lee thanks the Basic Science Research Program offered through the National Research Foundation of Korea (NRF) grant funded by the Korea government (MSIT) (NRF-2015R1C1A2A01055702 and NRF-2018R1A2B6007169).

References

1. M. Sagawa, S. Fujimura, N. Togawa, H. Yamamoto, Y. Matsuura, J. Appl. Phys. **55**, 2083 (1984)
2. G. Baia, R.W. Gao, Y. Sun, G.B. Han, B. Wang, J. Magn. Magn. Mater. **308**, 20 (2007)
3. M. Sagawa, S. Fujimura, H. Yamamoto, Y. Matsuura, S. Hirosawa, J. Appl. Phys. **57**, 4094 (1985)
4. W. Rodewald, B. Wall, M. Katter, K. Uestuener, IEEE Trans. Magn. **38**, 2955 (2002)
5. H. Chiriac, M. Grigoras, M. Urse, J. Appl. Phys. **101**, 09k523 (2007)
6. X.J. Cao, L. Chen, S. Guo, X.B. Li, P.P. Yi, A.R. Yan, G.L. Yan, J. Alloys Compd. **631**, 315 (2015)
7. T.T. Sasaki, T. Ohkubo, Y. Une, H. Kubo, M. Sagawa, K. Hono, Acta Mater. **84**, 506 (2015)
8. L. Liang, T. Ma, P. Zhang, J. Jin, M. Yan, J. Magn. Magn. Mater. **355**, 131 (2014)
9. Q. Wu, H. Ge, P. Zhang, N. Yu, A. Yan, Jpn. J. Appl. Phys. **53**, 053001 (2014)
10. J. Ni, M. Yan, T. Ma, W. Zhang, Mater. Chem. Phys. **515**, 126 (2015)
11. K. Uestuener, M. Katter, IEEE Trans. Magn. **42**, 2897 (2006)
12. J. Ju, X. Tang, R. Chen, J. Wang, W. Tin, D. Lee, A. Yan, Chin. Phys. B **24**, 017504 (2015)
13. L. Cai, S. Cuo, C. Yan, X. Zhang, R. Chen, L. Liu, D. Lee, A. Yan, IEEE Trans. Magn. **50**, 2103603 (2014)
14. U. Seelam, T. Ohkubo, T. Abe, S. Hirosawa, K. Hono, J. Alloys Compd. **617**, 884 (2014)
15. L.Q. Yu, M. Yan, J.M. Wu, W. Luo, X.G. Cui, H.G. Ying, Phys. B **393**, 1 (2007)
16. W. Pei, C. He, F. Lian, G. Zhou, H. Yang, J. Magn. Magn. Mater. **239**, 475 (2002)
17. L. Bo, H. Jifan, W. Dongling, G. Binglin, W. Xinlin, Rare Met. **23**, 152 (2004)
18. X. Jing, Y. Shihong, Y. Dunbo, L. Zongan, L. Shipeng, L. Hongwei, J. Rare Earths **24**, 306 (2006)
19. J. Bernardi, J. Fidler, M. Sagawa, Y. Hirose, J. Appl, Phys. **83**, 6396 (1998)
20. K. Loewe, C. Brombacher, M. Katter, O. Gutfleisch, Acta Mater. **83**, 248 (2015)
21. H. Kato, T. Miyazaki, M. Sagawa, K. Kotama, Appl. Phys. Lett. **84**, 4230 (2004)
22. M. Yue, J. Zhang, W. Liu, G. Wang, J. Magn. Magn. Mater. **271**, 346 (2004)
23. S. Guo, R. Chen, B. Zheng, G. Yan, D. Lee, A. Yan, IEEE Trans. Magn. **47**, 3267 (2011)
24. J. Wang, Y. Meng, H. Zhang, H. Tang, R. Lin, C. Sun, C. Wu, F. Xie, J. Magn. Magn. Mater. **396**, 283 (2015)
25. K. Lim, S. Park, S. Ahn, C. Kim, J. Kor. Phys. Soc. **63**, 1203 (2013)
26. B. Guo, B. Li, D. Wang, X. Yu, J. Hu, Mater. Sci. Forum **457–459**, 2169 (2005)
27. A. Sun, S. Wu, W. Xu, J. Wang, Q. Zhang, F. Zhai, A.A. Volinsky, Int. J. Miner. Metall. Mater. **19**, 236 (2012)
28. W. Liu, Z.D. Zhang, J.P. Liu, X.K. Sun, D.J. Sellmyer, X.G. Zhao, J. Magn. Magn. Mater. **221**, 278 (2000)
29. J. Bernardi, J. Fidler, M. Seeger, H. Kronmüller, IEEE Trans. Magn. **29**, 2773 (1993)
30. T. Hattori, N. Fukjamachi, R. Goto, N. Tezuka, S. Sugimoto, Mater. Trans. **50**, 479 (2009)
31. N.J. Yu, M.X. Pan, P.Y. Zhang, H.L. Ge, J. Magn. **18**, 235 (2013)
32. M. Daniila, H. Okumura, G.C. Hadjipanayis, D.J. Sellmyer, J. Magn. Magn. Mater. **267**, 316 (2003)
33. S.Z. Zhou, *Rare-Earth Permanent Magnet Materials and Their Applications* (Metallurgical Industry Press, Beijing, 1995), p. 128
34. K. Hono, H. Sepehri-Amin, Scr. Mater. **67**, 530 (2012)
35. J. Fidler, Y. Tawara, IEEE Trans. Magn. **24**, 1951 (1988)